Nanoscale Advances

ROYAL SOCIETY OF CHEMISTRY

PAPER

View Article Online
View Journal | View Issue

Cite this: *Nanoscale Adv.*, 2026, **8**, 224

Antioxidant potential and increased photocatalytic efficiency of gallic acid-capped ZnO and NiO NPs for azo dye degradation: effect of heterojunction coupling and machine learning-assisted modeling

Aqeela Sikandar,[a] Abu Bakar Siddique, *[a] Azhar Abbas,[ab] Abdul Majid,[c] Bilal Sikandar,[d] Muhammad Ashraf Shaheen,[e] Umar Nishan [f] and Khaled Fahmi Fawy[g]

This study presents the synthesis of gallic acid-capped zinc oxide nanoparticles (g-ZnO NPs), nickel oxide nanoparticles (g-NiO NPs), and their Z-scheme heterojunction nanocomposites (g-ZnO-NiO NCs) using a green approach with gallic acid as the reducing agent. Structural, morphological, and elemental analyses confirmed nanoscale crystallinity and uniform distribution, with effective ZnO–NiO coupling in the composite. XRD analysis revealed the minimum crystallite size of g-ZnO-NiO NCs (11.82 nm) in comparison to g-ZnO NPs (28.24 nm) and g-NiO NPs (17.93 nm). Photocatalytic performance was assessed for the degradation of crystal violet (CV) and Congo red (CR) dyes under solar light. Kinetic studies showed that g-ZnO-NiO NCs exhibited the highest degradation efficiencies (95% for CV and 92% for CR), with rate constant values (2.84×10^{-2} min^{-1} for CV and 2.56×10^{-2} min^{-1} for CR) significantly higher than those of individual g-ZnO and g-NiO NPs. The enhanced activity was attributed to efficient charge separation through a Z-scheme mechanism, facilitating the generation of $^{\bullet}O_2^-$ and $^{\bullet}OH$ radicals. Parameters such as pH, catalyst dose, dye concentration, and radical scavengers were optimized, confirming the role of reactive oxygen species in degradation process. Total organic carbon (TOC) analysis indicated significant mineralization (84% and 80% of CV and CR, respectively), and reusability tests showed high stability with a meager decrease of activity (~6%) over five cycles. Machine learning models, including Decision Tree, Random Forest, and ANN, accurately predicted the photocatalytic degradation process. The antioxidant assay results depicted the higher efficiency of g-ZnO-NiO NCs than pristine NPs and gallic acid, assessed by DPPH, TPC, and FRAP assays. Conclusively, it was emphasized that the g-ZnO-NiO heterojunction is a promising, sustainable photocatalyst for organic pollutant removal under solar irradiation and has better antioxidant potential than g-ZnO NPs, g-NiO NPs, and gallic acid.

Received 26th August 2025
Accepted 11th November 2025

DOI: 10.1039/d5na00827a

rsc.li/nanoscale-advances

1. Introduction

Direct mixing of untreated effluents of textile and pharmaceutical industries with freshwater reservoirs is a major cause of water pollution. Synthetic azo dyes, including crystal violet (CV) and Congo red (CR), are widely used in these industries as coloring agents and poses serious environmental risks due to their toxicity, carcinogenic properties, and resistance to biodegradation.[1–5] Among numerous remediation options, photocatalytic processes, like advanced oxidation processes (AOPs), are gaining significant attention. AOPs utilize the synergistic effect of semiconductors and light interaction to degrade azo dyes by the generation of reactive oxygen species (ROS).[6,7] Among semiconductor materials, zinc oxide (ZnO) and nickel oxide (NiO) nanoparticles (NPs) are extensively researched for their superior optical and electrical characteristics, elevated surface area, and chemical durability. However, there are a number of limitations that make it hard to use these materials widely, such as their stability in water, the rate at which charge carriers recombine, and particle size variability.[8–11]

[a]*Institute of Chemistry, University of Sargodha, Sargodha 40100, Pakistan. E-mail: abubakar.siddique@uos.edu.pk; abubakar054@gmail.com*

[b]*Department of Chemistry, Government Ambala Muslim College, Sargodha 40100, Pakistan*

[c]*Department of Botany, University of Sargodha, Sargodha 40100, Pakistan*

[d]*Department of Physics and Applied Mathematics, Pakistan Institute of Engineering and Applied Sciences (PIEAS), Nilore, Islamabad 45650, Pakistan*

[e]*Department of Allied Health Sciences, Superior University Lahore, Pakistan*

[f]*Department of Chemistry, Kohat University of Science and Technology, Kohat, 26000 KP, Pakistan*

[g]*Department of Chemistry, Faculty of Science, Research Center for Advanced Materials Science (RCAMS), King Khalid University, P.O. Box 960, Abha 61421, Saudi Arabia*

A major challenge with photocatalysis is that photogenerated electron–hole (e^-/h^+) pairs recombine very quickly, which reduces quantum efficiency and the formation of reactive species at a drastic rate.[12] Several studies have investigated methods to alleviate this issue, such as metal or nonmetal doping to create charge traps, oxygen vacancies, noble metal deposition, Type-II heterojunctions for spatial charge separation, and integration with carbon-based materials like g-C_3N_4 or graphene to enhance electron transport efficiency.[13,14] However, these often impact redox potential. The Z-scheme heterojunction overcomes this problem by imitating natural photosynthesis. It allows low-energy carriers to selectively recombine while keeping apart the highly oxidative holes and strongly reductive electrons. This improves charge separation, keeps redox activity constant, and boosts photocatalytic and biomedical performance. Therefore, the fabrication of heterojunctions between various semiconductors has garnered interest for its potential to enhance charge separation (e/h pairs) and augment photocatalytic performance.[15–18] The fabrication of Z-scheme heterojunctions can be carried out using various metal oxide NPs, like ZnO NPs and NiO NPs. In these NCs, the Z-scheme mechanism effectively maintains the robust redox potentials of both components while promoting efficient charge carrier separation, hence enhancing photocatalytic activity dramatically.[19,20]

In addition to photocatalysis, metal-based nanomaterials have also been reported for use in various fields, such as sensing biomolecules,[21] drug delivery,[22] hydrogen energy production,[23] iodine capture,[24] and biomedical applications.[25] The physicochemical properties and stability of nanomaterials for various applications are mainly determined by the nature of the nanomaterials and their surface functionalities. Generally, NPs and NCs synthesized *via* green methods are reported to be more stable and selective in their functions. Hence, several biomolecules have been used to synthesize NPs and improve their properties. In this regard, green synthesis employing plant-derived biomolecules such as gallic acid (GA) offers a sustainable alternative to conventional chemical methods.[26] Gallic acid, a naturally occurring polyphenol, is used in various biological applications as a bioactive agent or to improve the properties of biological agents by synergistic effects. For example, GA has been reported to enhance the antifungal properties of econazole in the form of a salt (econazolium–gallate–econazole)[27] and functions as both a reducing and a capping agent, contributing to increased surface stability, less agglomeration, and enhanced antioxidant and photocatalytic activity of the nanoparticles. GA capping also introduces surface functional groups that may contribute to dye adsorption, degradation pathways, and antioxidant applications.[28] Strong antioxidant activity is believed to be produced by the metal core through redox reactions, which interfere with free radicals and produce reactive oxygen species (ROS). However, the antioxidant potential is also increased due to the synergistic effect between NPs and GA. When combined, these NPs show strong antioxidant activity, which makes them attractive options for use in environmental protection, wound healing, and medicine.[29,30]

Optimization of degradation parameters may involve much time and resources *via* typical experimental approaches. By enabling the forecasting and analysis of complicated correlations between reaction conditions and degradation consequences, machine learning (ML) offers a strong alternative.[31] Machine learning models, such as Decision Trees, Artificial Neural Networks (ANN), and Random Forests, are very useful for improving complex systems because they can find hidden patterns and make accurate predictions. Decision Trees make it easier to understand how different factors affect decisions by showing how decisions are made visually. Artificial Neural Networks are great at capturing complicated, non-linear interactions, so they work well with data that has complicated patterns. By combining many decision trees, Random Forest makes predictions more accurate and reliable, reduces overfitting, and improves generalisation. These models work together to make photodegradation processes better, making sure that decisions are made quickly and accurately in challenging situations.[32,33]

Although the green synthesis of monometallic NPs using GA capping has been reported in the literature, the GA-based green synthesis of NCs has been studied scarcely. Therefore, in this study, the first-time synthesis of GA-capped ZnO–NiO NCs has been reported for improved photocatalytic and antioxidant potential. The GA-capped pristine ZnO NPs and NiO NPs, and g-ZnO-NiO NCs have been analyzed for photocatalytic efficacy to degrade CV and CR dyes under visible light irradiation. Owing to the superior activity of the g-ZnO-NiO NCs based on the development of a Z-scheme heterojunction, the effects of reaction parameters, pH, catalyst dose, initial dye concentration, and radical scavengers were also examined and optimized using ML tools. Various ML models were employed, like Decision Tree, Artificial Neural Network, and Random Forest, to train, validate, and predict the reaction parameters. The article demonstrates the dual role of gallic acid in NP production and performance enhancement, contributing to the development of sustainable materials for environmental cleanup.

2. Experimental

2.1. Materials and methods

The synthesis was carried out using high-purity analytical-grade chemicals procured from Sigma-Aldrich, Germany. Nickel nitrate hexahydrate ($Ni(NO_3)_2\cdot 6H_2O$), zinc nitrate hexahydrate ($Zn(NO_3)_2\cdot 6H_2O$), and gallic acid (GA; $C_7H_6O_5$) were used to make ZnO NPs, NiO NPs, and ZnO–NiO NCs, respectively. We used distilled water (DW) for all of the washing and solution-making steps. The Supplementary Information (Section S1) includes all the information about the instruments used for synthesis and characterization.

2.2. Synthesis of g-ZnO NPs, g-NiO NPs, and g-ZnO-NiO NCs

Using GA as a reducing and capping agent, GA-capped zinc oxide nanoparticles (g-ZnO NPs) were synthesized by a green approach. A 0.67 M solution of $Zn(NO_3)_2\cdot 6H_2O$ was prepared by dissolving 2 g of salt in 10 mL of water. Aqueous GA solution

(0.1 M, 0.17 g/10 mL) was added to the above solution with constant stirring for 10 minutes. The pH of the solution was adjusted to 9 by adding a 0.1 M solution of NaOH. The reaction mixture was heated to 85 °C and stirred continuously for 1 h. After the appearance of milky white precipitate, the mixture was cooled, followed by centrifugation at 6000 rpm for 30 min. The precipitates were washed with DW and dried at 80 °C for 2 h. Afterward, the precipitates were calcined at 350 °C for 3 h in a muffle furnace. The g-ZnO NPs obtained were cooled down and stored.

GA-capped nickel oxide nanoparticles (g-NiO NPs) were synthesized by mixing the nickel nitrate hexahydrate solution (0.67 M, 1.95 g/10 mL) with the GA solution (0.1 M, 0.17 g/10 mL) following the same procedure and conditions described above.

For the preparation of g-ZnO-NiO NCs, the separately prepared solutions of $Zn(NO_3)_2 \cdot 6H_2O$ (0.67 M, 2 g/10 mL) and $Ni(NO_3)_2 \cdot 6H_2O$ (0.67 M, 1.94 g/10 mL) were mixed, followed by the addition of GA solution (0.2 M, 0.34 g/10 mL) and adjusting the pH at 9 by adding 0.1 M NaOH with a constant stirring rate at 85 °C. After 2 hours, the precipitates were filtered off and calcined at 350 °C for 3 hours. The dark brownish color precipitates of g-ZnO-NiO NCs were collected and stored for further use.

2.3. Photodegradation of dyes

The photocatalytic activity of green-synthesized GA-capped g-ZnO NPs, g-NiO NPs, and g-ZnO-NiO NCs was evaluated for the degradation of CV and CR dyes under solar light, following the reported procedure.[10,34] A 10 ppm dye solution was prepared by dissolving 1 mg of dye in 100 mL of distilled water. For each experiment, a photocatalyst dose of 50 mg/20 mL was dispersed in the dye solution and stirred in the dark for 20 minutes to achieve adsorption–desorption equilibrium. A baseline UV-vis absorbance spectrum was recorded before exposure. The reaction mixtures were then irradiated under sunlight for 100 minutes, and absorbance was recorded at 10 minute intervals using a UV-visible spectrophotometer. Dye degradation was evidenced by the progressive fading of solution color and a decrease in absorbance intensity, as shown in Fig. 1a and b. The absorbance was measured at the dyes' maximum absorbance wavelengths (498 nm for CR (Fig. 1b) and 599 nm for CV (Fig. 1a)). For kinetic studies, $\ln(C_0/C_t)$ *versus* time was plotted to determine the rate constant (k) for the degradation reaction. Eqn (1) was used to determine the concentrations of dyes degraded.

$$\text{Degradation of azo dye}(\%) = \frac{A_0 - A_f}{A_0} \times 100 \quad (1)$$

Here, A_0 and A_f represent the initial and the final absorbance of solutions, respectively.

2.4. Effect of reaction parameters (pH, initial dye concentration, catalyst dose, and radical scavengers) on dye degradation

The effect of reaction mixture pH on dye degradation was examined by altering the pH of the dye solution (2, 4, 6, 8, 10, and 12), utilising 0.1 M HCl or 0.1 M NaOH. For every batch reaction, the catalyst dose (50 mg/20 mL) was added to the dye solution, followed by 20 minutes of stirring and then exposure to sunlight for 100 minutes. The degradation (%) was monitored by continuously recording the UV-vis spectroscopic absorbance data.

To evaluate the initial dye concentration effect on degradation, dye solutions with concentrations of 10, 20, 30, 40, and 50 ppm were prepared. Each sample solution (20 mL) was mixed with 50 mg of the photocatalyst and stirred in the dark for 20 minutes to establish adsorption–desorption equilibrium. The mixtures were then exposed to sunlight and dye degradation was monitored spectrophotometrically.

To study the effect of catalyst dosage, varying amounts of the synthesized nanocatalyst (5–70 mg/20 mL) were added to a 10 ppm solution of each dye. The same procedure as described above was used to evaluate the degradation efficiency of each batch reaction.

To examine the role of dominant ROS in the photocatalytic process on the surface of the nanocatalyst, different radical scavengers were used: isopropanol (IPA) for hydroxyl radicals ($^{\bullet}OH$), *p*-benzoquinone (*p*-BQ) for superoxide radicals ($^{\bullet}O_2^-$),

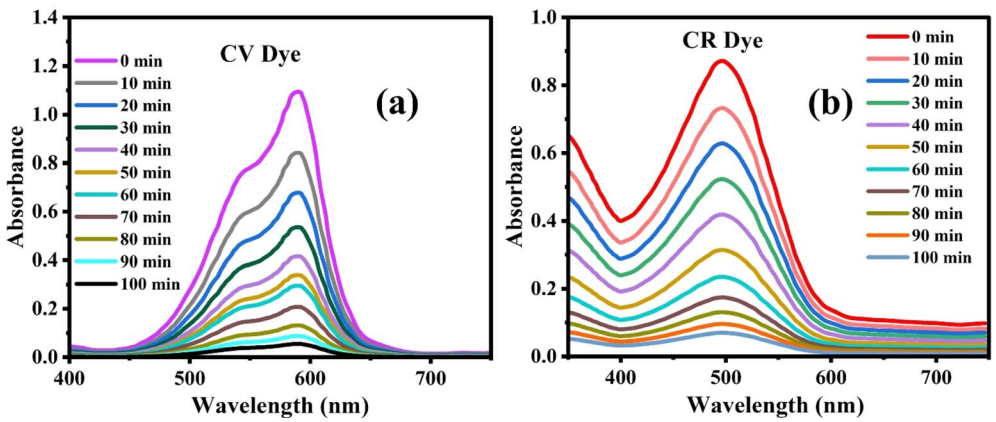

Fig. 1 Absorbance spectra of dye at different time intervals: (a) CV dye and (b) CR dye.

Na_2EDTA for photogenerated holes (h^+), and L-ascorbic acid for hydrogen peroxide (H_2O_2). Each scavenger (1 mM, 10 mL) was added to the dye–catalyst suspension before exposure to sunlight. The same procedure as described above was used to evaluate the degradation efficiency of each batch reaction.

2.5. ML tool-based modelling and optimization

All machine learning operations were carried out on the Kaggle computational platform, which offers a Python environment equipped with widely used libraries such as scikit-learn, pandas, NumPy, and Matplotlib. A structured pipeline framework was developed to maintain consistency and reproducibility across preprocessing, model training, and evaluation stages. During preprocessing, numerical features were standardized, and categorical variables were encoded to ensure uniformity throughout the dataset. The decision tree regressor, random forest regressor, support vector regressor with an RBF kernel, and an ANN implemented as a multilayer perceptron regressor were among the machine learning techniques utilized for model training. Leave-One-Out Cross-Validation (LOOCV) was performed during training to guarantee that the models were well-fitted and to enhance the trustworthiness of the results.

Three regularly used error metrics – the mean absolute error (MAE), the root mean square error (RMSE), and the coefficient of determination (R^2) – were then used to evaluate the prediction effectiveness of these models. After defining the evaluation metrics, the structural operations of the applicable ML models are described to allow a better comprehension of their structures.

ANN modelling is considered a better option over traditional models, like regression or response surface models, because it does not depend on predefined functional relationships and can accurately model systems that are nonlinear, multidimensional, and very interactive. Also, ANNs learn directly from data, which makes them more accurate at predicting things, more adaptable to new situations, and more flexible in experimental fields that are complicated or unclear.[35] The ANN (MLP Regressor) workflow comprises an output layer that predicts the target variable, one or more hidden layers that conduct nonlinear transformations, and an input layer that receives the data. To reduce the disparity between anticipated and experimental values, the network learns by altering its weights using backpropagation. This design (Fig. 2) permits the modelling of the dataset's complicated and nonlinear interactions.

The Decision Tree model (Fig. 3) separates the information continually depending on feature values to minimize prediction error at each node. While core nodes represent decision rules generated from the input features, leaf nodes give the final predicted values. This format makes it easy to comprehend how features affect the target variable.

2.6. DPPH, FRAP and TPC assays

The antioxidant potential of g-ZnO NPs, g-NiO NPs, and g-ZnO-NiO NCs was evaluated by DPPH (1,1-diphenyl-2-picrylhydrazyl) radical scavenging assay, total phenolic content (TPC), and

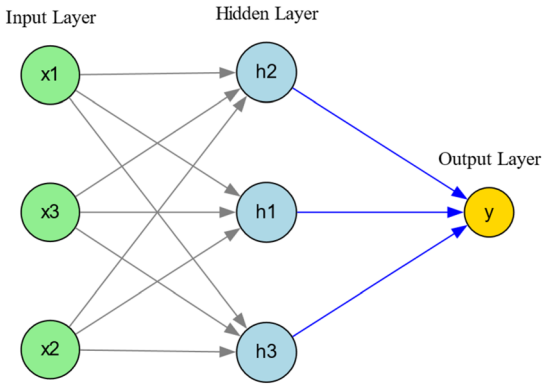

Fig. 2 The ANN (MLP Regressor) showing the connected input, hidden, and output layers.

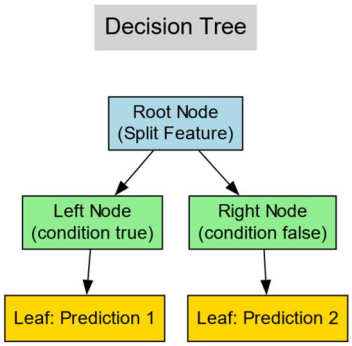

Fig. 3 The Decision Tree Regressor's workflow, illustrating the hierarchical structure of the decision nodes and leaves.

FRAP (ferric reducing antioxidant power) assay, following the reported procedure.[36,37] The detailed description of antioxidant assays is explained in Supplementary Information S2.

2.7. Statistical significance

All photocatalytic studies were performed in triplicate, and the data are reported as mean ± standard deviation (SD). Statistical analysis was performed using ANOVA, with a significance level set at $p < 0.05$.

3. Results and discussion

The use of GA as both a capping and a reducing agent played a key role in the green synthesis process. It regulates the nucleation and growth of NPs, leading to a uniform size distribution, an optimized energy bandgap, and improved crystallinity. This eco-friendly approach not only enhanced the stability and dispersion of the material but also aligned with the principles of green chemistry, making the synthesized nanoparticles promising candidates for sustainable photocatalytic applications.[29]

3.1. XRD analysis

X-ray diffraction (XRD) analysis was performed to investigate the crystalline structure and phase composition of g-ZnO NPs,

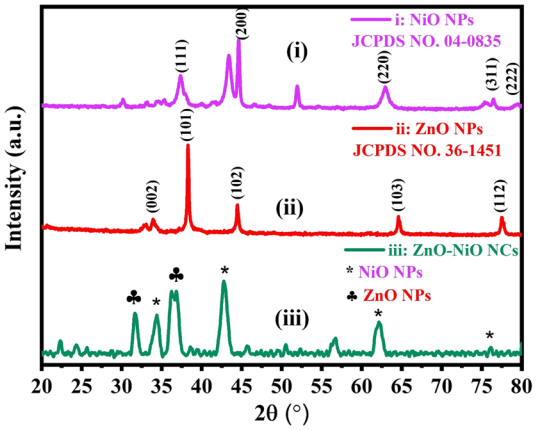

Fig. 4 XRD spectra of (i) g-NiO NPs, (ii) g-ZnO NPs, and (iii) g-ZnO-NiO NCs.

g-NiO NPs, and g-ZnO-NiO NCs. The XRD pattern of g-ZnO NPs revealed characteristic peaks at 2θ values of approximately 31.7°, 34.4°, 36.2°, 47.5°, 56.6°, 62.8°, and 68.0°, which correspond to the (100), (002), (101), (102), (110), (103), and (112) crystal planes, as shown in Fig. 4(ii). These diffraction peaks are in excellent agreement with the hexagonal wurtzite structure of ZnO and match well with the standard JCPDS Card No. 36-1451. The sharpness and intensity of the peaks indicate the high crystallinity of the synthesized g-ZnO NPs.[38,39]

Similarly, the XRD pattern of the g-NiO NPs exhibited prominent peaks at 2θ values of around 37.2°, 43.3°, 62.8°, 75.4°, and 79.4°, which are indexed to the (111), (200), (220), (311), and (222) planes of the cubic phase of NiO, confirming successful synthesis of phase-pure NiO NPs, as shown in Fig. 4(i). These peaks correspond to the standard JCPDS Card No. 04-0835 and indicate a well-crystallized structure of g-NiO NPs.[40]

For the g-ZnO-NiO NCs, the XRD pattern (Fig. 4(iii)) demonstrated a combination of diffraction peaks from both ZnO NPs and NiO NPs, validating the formation of a binary nanocomposite. The presence of distinct peaks from both components suggests that g-ZnO NPs and g-NiO NPs retained their respective crystalline structures without forming any secondary phases, supporting the successful fabrication of a heterojunction system. The coexistence of hexagonal ZnO and cubic NiO in the composite structure is essential for the formation of a Z-scheme heterojunction, which is beneficial for enhanced photocatalytic performance.

The crystallite characteristics of the nanomaterials were estimated using eqn (2)–(4), as illustrated in the literature.[41–44] The values of crystallite parameters are displayed in Table 1. The crystallite characteristics of g-ZnO NPs, g-NiO NPs, and g-ZnO-NiO NCs revealed distinct structural differences that significantly influence their potential applications. The g-ZnO NPs possessed the largest crystallite size (28.24 nm), accompanied by the lowest dislocation density (1.25×10^{-3} nm^{-2}) and microstrain (0.42×10^{-3}), indicating a more stable and less defective crystal structure. In contrast, the g-NiO NPs exhibited a smaller crystallite size (17.93 nm) along with a higher dislocation density (3.11×10^{-3} nm^{-2}) and microstrain (0.62×10^{-3}), suggesting a greater concentration of structural defects and internal strain relative to ZnO. The g-ZnO-NiO nanocomposites (NCs) displayed the smallest crystallite size (11.82 nm) and the highest dislocation density (7.06×10^{-3} nm^{-2}) and microstrain (1.50×10^{-3}), reflecting pronounced lattice distortions at the ZnO–NiO interface. Such an increase in structural imperfections and strain within the NCs indicated a highly reactive surface, which can enhance catalytic activity, charge carrier separation, and overall reactivity in applications such as photocatalysis and sensing. Consequently, the synthesis of g-ZnO-NiO NCs resulted in a defect-rich material with promising potential for advanced technologies that benefit from elevated surface activity.

Table 1 Crystallite parameters of g-ZnO NPs, g-NiO NPs and g-ZnO-NiO NCs

Nanomaterial	Crystallite size (nm)	Dislocation density ($\theta \times 10^{-3}$) (nm^{-2})	Microstrain ($\varepsilon \times 10^{-3}$)
g-ZnO NPs	28.24	1.25	0.42
g-NiO NPs	17.93	3.11	0.62
g-ZnO-NiO NCs	11.82	7.06	1.50

$$D = \frac{k\lambda}{\beta \cos\theta} \quad (2)$$

$$\delta = \frac{1}{D^2} \quad (3)$$

$$\varepsilon = \frac{\beta}{4 \tan\theta} \quad (4)$$

3.2. FTIR and ZP analysis

The FTIR spectra (Fig. 5a) provided insight into the functional groups present on the surface of the GA-capped g-ZnO, g-NiO NPs, and g-ZnO-NiO NCs. The broad absorption band observed around 3400 cm^{-1} in all samples corresponds to the O–H stretching vibrations, indicating the presence of hydroxyl groups from GA. The characteristic band around 1700 cm^{-1} was attributed to the C=O stretching vibration, confirming the presence of carboxyl groups from GA, which play a crucial role in stabilizing and capping the nanoparticles. Bands appearing in the region of 500–700 cm^{-1} were associated with metal–oxygen (M–O) vibrations: Zn–O in the case of g-ZnO NPs, Ni–O for g-NiO NPs, and both for g-ZnO-NiO NCs.[45,46] Some additional bands (1000–600 cm^{-1}) in the FTIR spectra might be attributed to the presence of Zn–O–Zn and Ni–O–Ni bonds in the nanostructures, as supported by the literature.[46,47] The successful incorporation of these functional groups confirmed that GA not only acted as a reducing agent but also as a stabilizing agent during green synthesis.

Zeta potential analysis (Fig. 5b–d) was conducted to evaluate the surface charge and colloidal stability of the synthesized nanostructures. The measured zeta potentials were −31.25 mV for g-ZnO NPs, −25.92 mV for g-NiO NPs, and −30.09 mV for the

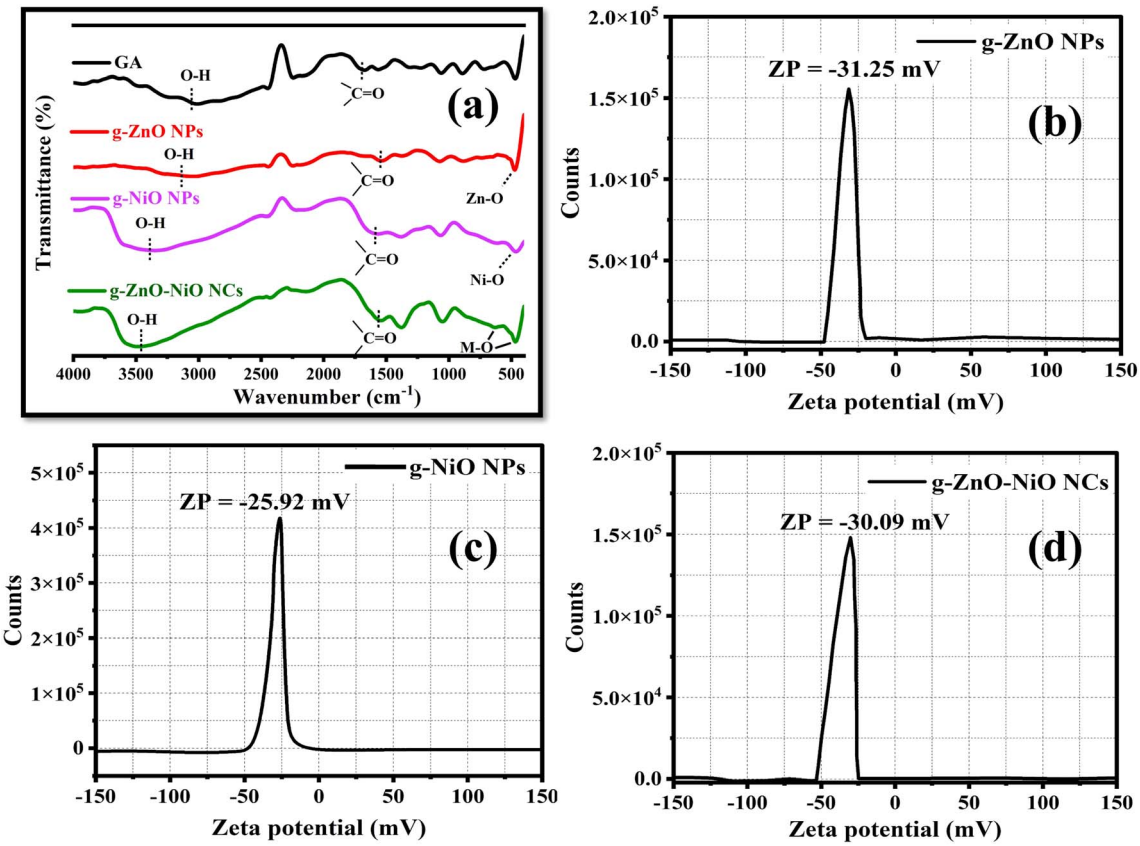

Fig. 5 (a) Comparative FTIR spectra of gallic acid, g-ZnO NPs, g-NiO NPs, and g-ZnO-NiO NCs, (b) ZP of g-ZnO NPs, (c) ZP of g-NiO NPs, and (d) ZP of g-ZnO-NiO NCs.

g-ZnO-NiO NCs. These significantly negative values indicated good colloidal stability and strong electrostatic repulsion among particles, which prevents agglomeration. The high surface charge was primarily attributed to the presence of ionizable groups from gallic acid, confirming effective capping. Notably, the slightly lower zeta potential of the g-NiO NPs compared to g-ZnO NPs suggested a variation in surface interaction between GA and metal oxide surfaces. The g-ZnO-NiO NCs exhibited a zeta potential value close to that of g-ZnO, indicating stable composite formation with retained surface charge characteristics, which contributes to enhanced dispersion and photocatalytic performance.

3.3. Optical properties of NPs and NCs

The UV-visible absorption and Tauc plot analyses offer significant insights into the optical characteristics and band structure of g-ZnO NPs, g-NiO NPs, and g-ZnO-NiO NCs. The UV-vis spectra of g-ZnO NPs (Fig. 6a(ii)) showed a clear absorption edge around 358 nm, depicting a wide band gap. The g-NiO NPs (Fig. 6a(i)) had an absorption peak close to 288 nm, and the g-ZnO-NiO NCs (Fig. 6a(iii)) had an absorption edge around 317 nm. The change in the absorption edge for the NCs implies that ZnO and NiO interact strongly with each other electronically, which confirms that a heterojunction has formed that improves the absorption of visible light. In addition to the shifting, the g-ZnO-NiO NC peak was also relatively broader than that of pristine NPs, indicating the wide sunlight absorbing potential and visible light responsiveness of NCs. A similar trend has been reported previously for Z-scheme heterojunctions.[48]

Tauc plot analysis further validated the optical properties by calculating the band gaps of the synthesized nanomaterials.[49] The Tauc plot of the sample was plotted utilizing eqn (5), where α, h, ν, and B denoted the molar extinction coefficient, Planck's constant, frequency, and proportionality constant, and n represents the nature of electron transition ($n = 1/2$) for direct transitions.

$$(\alpha h\nu)^{\frac{1}{n}} = B(h\nu - E_g) \quad (5)$$

The g-ZnO NPs (Fig. 6b) exhibited a direct band gap of 3.15 eV, while g-NiO NPs (Fig. 6c) showed a slightly narrower band gap of 2.78 eV, indicating better absorption in the visible range. Importantly, the g-ZnO-NiO NCs (Fig. 6d) demonstrated a reduced band gap of 2.90 eV, falling between that of pure g-ZnO NPs and g-NiO NPs. The narrowing of the band gap in the NCs was due to the two metal oxides working together, which makes it easier to separate charges and increases photocatalytic efficiency. Conclusively, the optical characterization supported that the incorporation of NiO with ZnO not only

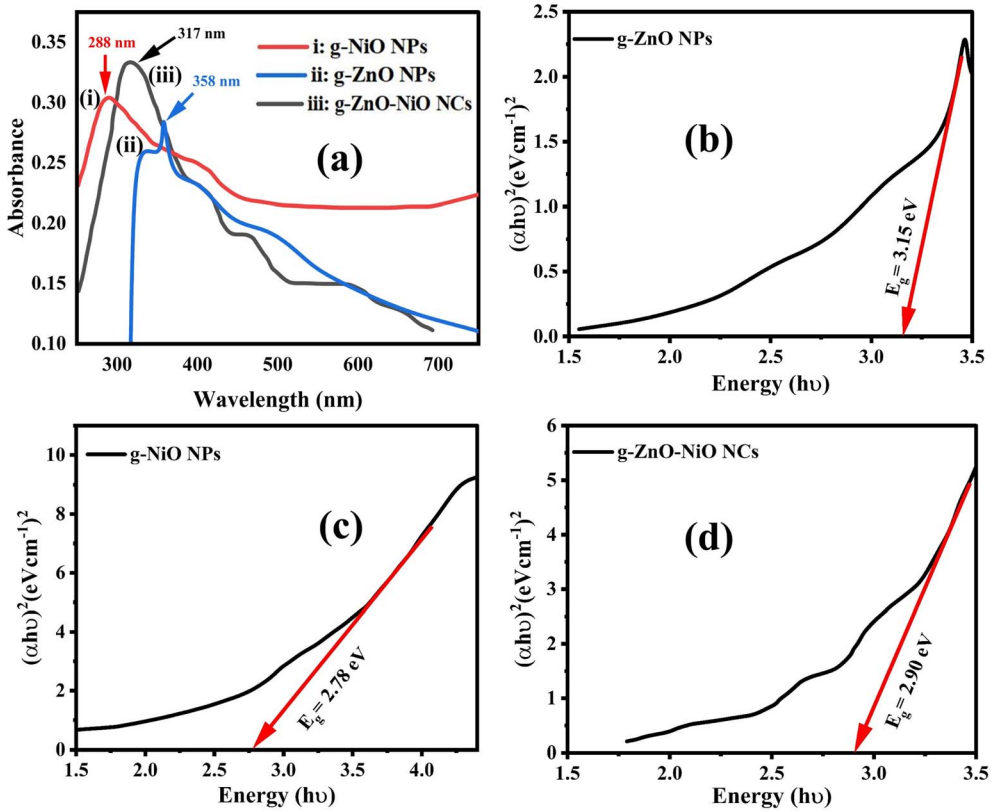

Fig. 6 (a) UV-vis spectrum of g-NiO NPs (i), g-ZnO NPs (ii), and g-ZnO-NiO NCs (iii), (b) Tauc plot of g-ZnO NPs, (c) Tauc plot of g-NiO NPs, and (d) Tauc plot of g-ZnO-NiO NCs.

improves visible light responsiveness but also optimizes the electronic structure through the formation of a Z-scheme heterojunction. This made the g-ZnO-NiO NCs a promising candidate for efficient solar-driven photocatalytic applications.

3.4. SEM and EDX analyses

The SEM, particle size distribution histogram, and EDX analyses collectively confirm the morphology, size, and elemental composition of the g-ZnO NPs, g-NiO NPs, and g-ZnO-NiO NCs. Generally, it has been observed that with a decrease in particle size in nanomaterials, the surface area increases, resulting in a larger number of active sites on the catalyst and improved photocatalytic activity. More interaction of the pollutant with the catalyst surface results in better adsorption on the surface and more generation of ROS for redox reactions.[50]

In the SEM images, g-ZnO NPs (Fig. 7a) appeared as agglomerated granular particles with a relatively uniform distribution. Their corresponding particle size distribution histogram (Fig. 7b) showed an average size of 78.9 ± 12.3 nm, indicating moderate uniformity in NP dimensions. The EDX spectrum (Fig. 7c) confirmed the presence of Zn and O as major elements, validating the formation of g-ZnO NPs with high purity.

The g-NiO NPs (Fig. 7d) exhibit a slightly more irregular morphology with dense packing of the particles. The particle size distribution histogram (Fig. 7e) showed a wider range of particle sizes, with an average size of 86.6 ± 16.1 nm. EDX analysis (Fig. 7f) showed strong peaks for Ni and O, as well as weak signals for Cl, Na, Si, S, and Ca. These weak signals might have occurred due to trace impurities.

The SEM image of the g-ZnO-NiO NCs (Fig. 7g) showed a more compact, embedded shape that is typical of NCs. The histogram of particle size distribution (Fig. 7h) showed that the average size was 75.5 ± 16.7 nm, which means that both oxides were successfully combined at the nanoscale. The EDX spectrum (Fig. 7i) displays distinct peaks for Zn, Ni, and O, affirming the successful synthesis of the composite material containing both ZnO and NiO phases.

3.5. Photocatalytic activity of g-ZnO NPs, g-NiO NPs, and g-ZnO-NiO NCs

The photocatalytic performance of g-ZnO NPs, g-NiO NPs, and g-ZnO-NiO NCs was systematically evaluated against crystal violet (CV) and congo red (CR) dyes under solar irradiation. As shown in Fig. 8a and b, all materials demonstrated progressive dye degradation with increasing irradiation time; however, g-ZnO-NiO NCs exhibited the highest efficiency, achieving ~95% CV and ~92% CR degradation within 100 min. In contrast, g-ZnO NPs and g-NiO NPs showed comparatively lower degradation efficiencies, indicating the synergistic effect of the heterojunction in the nanocomposite.

The kinetics of the degradation reaction were studied using the Langmuir–Hinshelwood mechanism (eqn (6)), which demonstrates the dependence of the rate constant on the

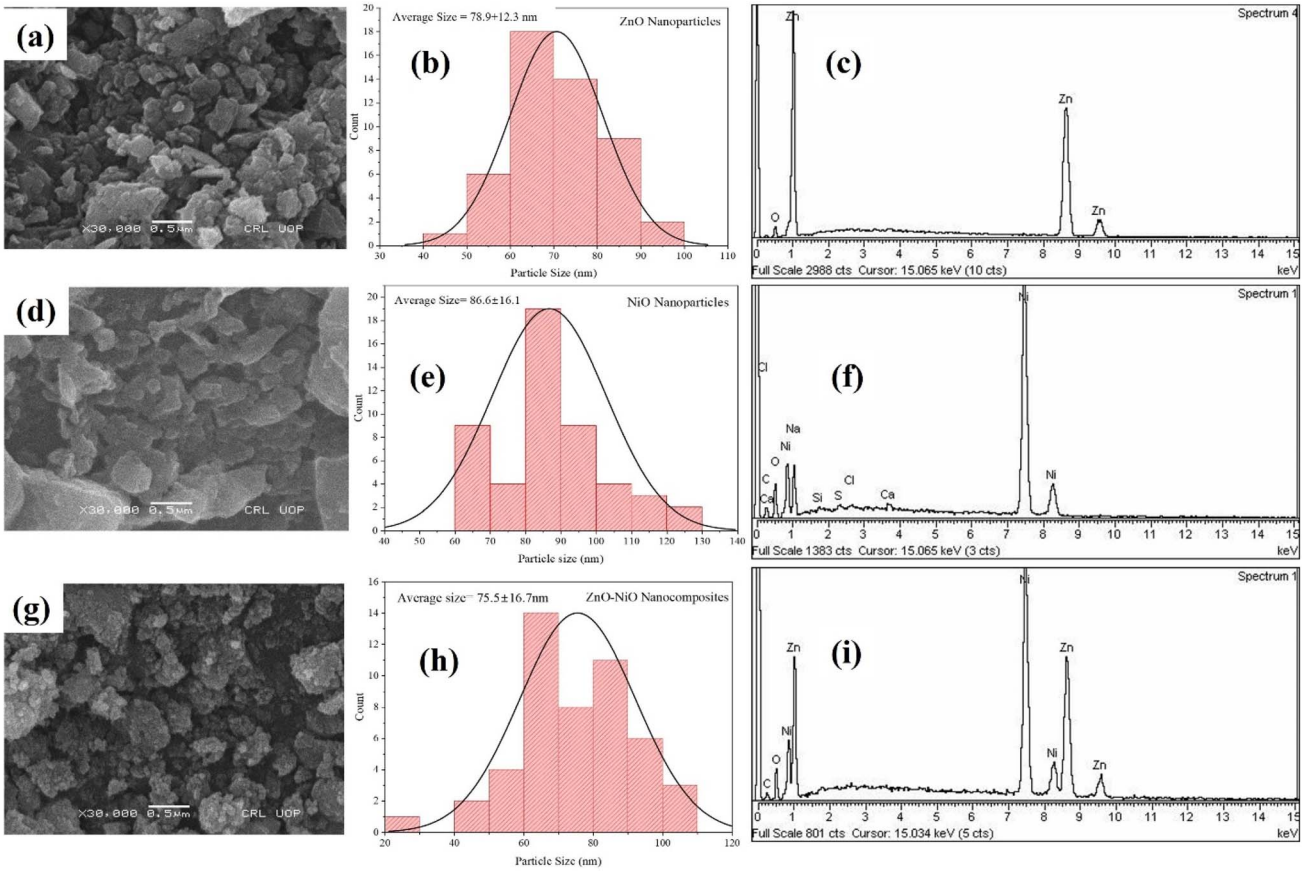

Fig. 7 (a) SEM image of g-ZnO NPs, (b) particle size histogram of g-ZnO NPs, (c) EDX spectrum of g-ZnO NPs, (d) SEM image of g-NiO NPs, (e) particle size histogram of g-NiO NPs, (f) EDX spectrum of g-NiO NPs, (g) SEM image of g-ZnO-NiO NCs, (h) particle size histogram of g-ZnO-NiO NCs, and (i) EDX spectrum of g-ZnO-NiO NCs.

concentration of the pollutant and surface coverage of the catalyst.[51]

$$\text{Rate of reaction} = -\frac{dC}{dt} = k_r\theta = \frac{k_r KC}{1 + KC} \quad (6)$$

Here, k_r, K, θ, and C represent the reaction rate constant, reactant adsorption constant, fraction of catalyst surface coverage, and pollutant concentration at time t. Since the concentration of dyes is very low, the rate of degradation is mainly dependent on the concentration of the pollutant and eqn (6) cancer equation (eqn (7) and (8)).

$$-\frac{dC}{dt} = kt \quad (7)$$

On integration,

$$\ln\left(\frac{C_0}{C_t}\right) = kt \quad (8)$$

Here, C_0 and C_t represent the initial and final concentrations of CV and CR dyes after time 't'. By plotting $\ln(C_0/C_t)$ *vs.* t, the kinetic analysis (Fig. 8c and d) revealed that the degradation followed pseudo-first-order kinetics for both dyes, with the highest rate constants (k) observed for g-ZnO-NiO NCs – 2.84×10^{-2} min^{-1} for CV and 2.56×10^{-2} min^{-1} for CR – significantly higher than those for g-ZnO NPs (1.42×10^{-2} min^{-1} for CV; 1.37×10^{-2} min^{-1} for CR) and g-NiO NPs (1.33×10^{-2} min^{-1} for CV; 1.19×10^{-2} min^{-1} for CR). The superior activity of g-ZnO-NiO NCs can be attributed to enhanced charge separation and preservation of strong redox potentials *via* a Z-scheme electron transfer pathway. Furthermore, GA-capping played a dual role: it enhances the dispersion and stability of the NPs and provides surface functional groups that facilitate dye adsorption and interaction with reactive radicals. This combination of efficient charge carrier dynamics, preserved redox potential, and surface-mediated adsorption–reaction synergy accounted for the markedly superior photocatalytic activity of g-ZnO-NiO NCs compared to their single-component counterparts.

3.6. Effect of pH, catalyst dose, initial dye concentration, and radical scavengers

The photocatalytic efficiency of g-ZnO-NiO NCs toward CV and CR dyes was strongly influenced by pH (Fig. 9a). pH affects the adsorption efficiency of the dye molecules on the surface of the catalyst. Since the catalyst's surface is negatively charged, as indicated by the ZP value, the adsorption of the dyes must increase with a decrease in pH.[52,53] But experimentally, it was observed that the dye degradation increased progressively from acidic to slightly alkaline media, with maximum removal (95%

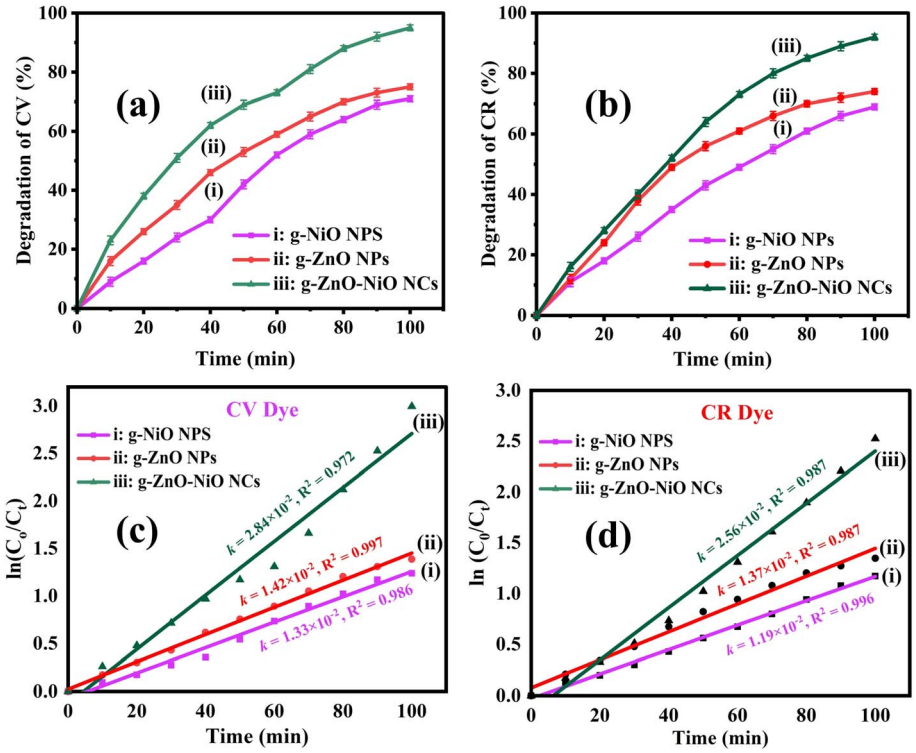

Fig. 8 Degradation of dye on the surface of g-NiO NPs (i), g-ZnO NPs (ii), and g-ZnO-NiO NCs (iii): (a) CV dye and (b) CR dye; and kinetics plot of degradation of (c) CV dye and (d) CR dye under optimum reaction conditions (10 ppm initial dye concentration, 50 mg/20 mL catalyst dose, and pH 8).

for CV, 92% for CR) observed at pH 8. Under acidic conditions (pH 2–4), degradation efficiency dropped significantly due to protonation of dye molecules, capture of radicals and electrons by hydronium ions, and surface charge alteration of the catalyst, which hindered electrostatic adsorption. At higher alkaline pH (>8), a slight decline was observed, possibly due to OH^- oversaturation leading to recombination of photogenerated electron–hole pairs. These findings are consistent with reports that optimal pH enhances surface hydroxyl radical formation and dye–catalyst interaction.[3]

Catalyst dosage also had a pronounced effect on dye degradation, as shown in Fig. 9b. An increase from 5 mg to 50 mg improved degradation efficiency, attributed to the availability of more active sites for dye adsorption, photon absorption, and reactive species generation, as described in the literature.[54] Beyond 50 mg, a marginal decrease occurred, likely due to excessive turbidity and light scattering, which reduced light penetration and photon utilization efficiency.[55]

The initial dye concentration study (Fig. 9c) revealed that the highest removal rates occurred at 10 ppm (95% CV, 92% CR). Generally, the rate of removal of pollutants increases with an increase in concentration due to an increase in collisional probability between pollutant molecules and catalysts. However, after optimal concentration, the degradation efficiency is decreased due to the turbidity of the solution in photocatalytic systems.[56,57] Therefore, the increase of dye concentration from 10 ppm to 50 ppm decreased degradation efficiency. This reduction is ascribed to increased competition of dye molecules for active sites and reduced light transmittance in more concentrated solutions, leading to lower reactive radical generation per dye molecule. Similar trends have been reported for other semiconductor photocatalysts.[49]

Radical scavenger experiments (Fig. 9d) provided mechanistic insights into the degradation pathway.[58] Addition of L-ascorbic acid (L-AA, an $O_2^{\bullet-}$ scavenger) reduced degradation to ~59% (CV) and ~57% (CR), while Na_2EDTA (a hole scavenger) caused the most significant decrease (~43% CV, ~38% CR), indicating that photogenerated holes (h^+) played a dominant role. Isopropanol ($^{\bullet}OH$ scavenger) and *p*-benzoquinone (*p*-BQ, $O_2^{\bullet-}$ scavenger) also reduced efficiency, confirming that both hydroxyl radicals and superoxide radicals participate in dye degradation. The pronounced effect of Na_2EDTA suggests that the Z-scheme heterojunction of g-ZnO-NiO NCs effectively preserves high oxidation potential in the valence band of NiO, enabling hole-driven generation of $^{\bullet}OH$ radicals.

To further verify the generation of ROS and electron transfer in NCs, the band edge positions of g-ZnO NPs and g-NiO NPs were calculated using the Butler-Ginley method (explained in Supplementary Information S3), which revealed that both oxides possess valence bands sufficiently positive to drive oxidative processes, while their conduction bands have relatively positive potentials for superoxide generation. g-ZnO NPs, with a band gap of 3.14 eV, exhibited valence and conduction band potentials of approximately +2.86 V and −0.28 V *vs.* NHE, respectively. In contrast, g-NiO NPs, with a narrower band gap of 2.78 eV, showed corresponding potentials of +2.49 V and −0.29 V *vs.* NHE. These

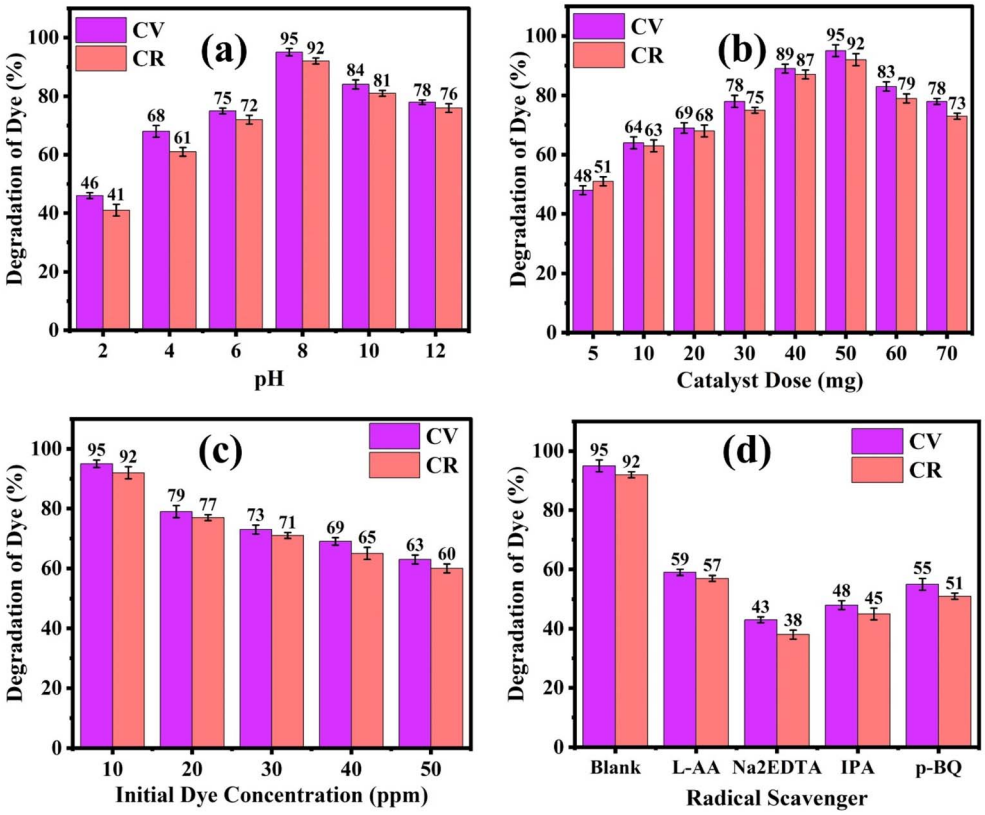

Fig. 9 Effect of (a) pH, (b) catalyst dosage, (c) initial dye concentration, and (d) radical scavengers on dye degradation.

positive valence band positions exceed the oxidation potential of the hydroxyl radical formation reaction ($OH^{\bullet}/OH^{-} \approx +2.44$ V *vs.* NHE at pH 7), enabling photogenerated holes to oxidize surface hydroxyl ions or water molecules to highly reactive $OH^{\bullet}$ radicals. However, since their conduction band potentials are more positive than −0.33 V *vs.* NHE, the threshold required to reduce molecular oxygen to superoxide radicals ($O_2^{\bullet -}$), the photogenerated electrons in both g-ZnO NPs and g-NiO NPs lack sufficient reducing power to initiate this reaction. Consequently, under illumination, these materials predominantly facilitate oxidative pathways involving h^+ and $OH^{\bullet}$ generation, while the formation of superoxide radicals remains thermodynamically unfavorable. However, from the experimental results (Fig. 9d), it can be observed that all the ROS, including $O_2^{\bullet -}$, were produced on the interface of g-ZnO-NiO NCs that strongly supported the appropriate band alignment of the oxides in the NCs.

Based on radical scavenging experiments, a Z-scheme mechanism of electron transfer was proposed in the g-ZnO-NiO NCs, as shown in Fig. 10. The proposed Z-scheme mechanism involved solar-light-induced excitation of electrons, generating electron–hole pairs in NCs, and the electrons from the CB of one material are transferred to the VB of other materials, resulting in the better charge separation of electrons in the CB of the 2nd material and h^+ in the VB of the 1st material.[35,59,60] In the heterojunction, photogenerated electrons in the CB of ZnO recombine with photogenerated holes in the VB of NiO at the interface. This selective recombination results in the highly reducing electrons in the CB of NiO (E_{CB} more negative) and the strongly oxidizing h^+ in the VB of ZnO (E_{VB} more positive). The retained electrons in NiO can effectively reduce dissolved oxygen to $^{\bullet}O_2^{-}$, while the holes in ZnO oxidize water or hydroxide ions to hydroxyl radicals ($^{\bullet}OH$). These ROS act synergistically to break down dye molecules into smaller, less toxic products, leading to effective mineralization. Hence, the optimal photocatalytic performance at pH 8, 50 mg catalyst dose, and 10 ppm dye concentration, combined with ROS results, confirmed that the degradation mechanism followed a Z-scheme charge transfer pathway, where synergistic action of h^+, $O_2^{\bullet -}$, and $^{\bullet}OH$ radicals drives efficient breakdown of CV and CR dyes under solar irradiation. The proposed degradation mechanism is illustrated in Supplementary Information S4. Briefly, the degradation mechanism of azo dyes on g-ZnO-NiO NCs under sunlight occurs *via* a Z-scheme photocatalytic route involving the following steps. Firstly, on exposure to solar irradiation, both g-ZnO NPs and g-NiO NPs absorb photons, resulting in the generation of e^-/h^+ pairs. These active charge carriers then drive a chain of redox reactions at the catalyst surface. The h^+ in ZnO's VB oxidize adsorbed water or hydroxyl ions to produce $^{\bullet}OH$ and hydronium ions, while the electrons in NiO's CB convert O_2 to $O_2^{\bullet -}$. The $O_2^{\bullet -}$ can further change into hydroperoxyl radicals ($HO_2^{\bullet}$) and hydrogen peroxide (H_2O_2), which break down into more $^{\bullet}OH$ radicals, intensifying the oxidative environment. These ROS, along with direct hole oxidation, attacked the dye molecules. This resulted in intermediate intermediates, and in the end, the dye was fully mineralized into CO_2 and H_2O. So, the synergistic charge transfer

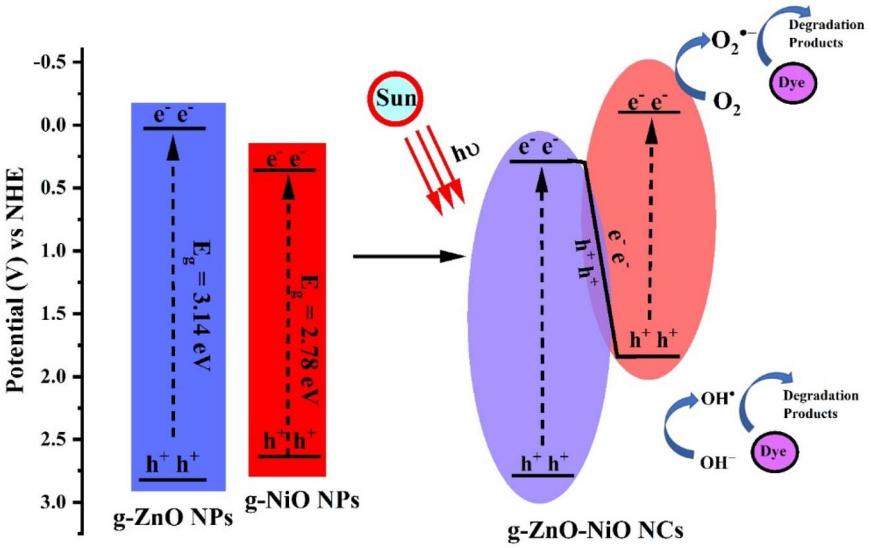

Fig. 10 Proposed Z-scheme heterojunction based on g-ZnO NPs and g-NiO NPs.

in the g-ZnO-NiO NCs enhanced carrier separation, maintained simultaneous oxidation and reduction events, and explained why azo dyes break down so well in sunlight.

3.7. ML-assisted modelling and optimization of dye degradation

ML models were applied to predict the performance of the photocatalytic degradation of different experimental conditions. The study was done on two dyes, CV and CR. The three parameters – pH, dose of catalyst, and initial dye concentration – were manipulated independently, whilst the remaining parameters were kept constant. In both cases, graphs were used to compare the experimental predictions and model predictions. These three parameters were tested together *via* Leave-One-Out Cross-Validation (LOOCV) in order to ensure that the model evaluation was correct. Various statistical parameters, like R^2, RMSE, and MAE, were analyzed to understand the level of accuracy of each model quantitatively. In order to determine the effect pH has on ML, the pH was varied with a constant dosage of catalyst and initial concentration of dye. Keeping the other parameters constant, the ML models were configured to forecast the degree of degradation over the test range of the pH values, and then the results were plotted against the actual results. Table S1 provides a summary of the data employed in the case. The data set was divided into three parts, which were a training set (70%), a testing set (15%), and a validation set (15%). This was done so that the network could learn, be tested, and be validated. The models were compared to each other to assess the suitability for prediction, as indicated in Table 2 and Fig. S1.

To further verify the model's reliability, predictions were examined under the optimized conditions (catalyst dose: 50 mg, pH: 8, and initial concentration: 10 ppm) to assess the accuracy of the decision tree model. Table 3 illustrates a comparison of the predicted and experimentally observed degradation efficiencies of CV and CR dyes under optimized pH conditions utilizing the decision tree model. The model demonstrated robust predictive accuracy, exhibiting a minimal difference of 1.5% between projected and actual values for both dyes, hence affirming its dependability in forecasting photocatalytic degradation performance.

To better demonstrate the predictability of the highest-performing as well as second-best model, an actual *vs.* predicted degradation graphs were also plotted, as shown in Fig. 11a (Decision Tree model) and Fig. 11b (ANN model).

To analyze the effect of catalyst dose, the catalyst dose was changed in the range of 5–70 mg, while keeping the other parameters constant. The dataset has 16 rows and 6 columns, with the dose of the catalyst changed and all the other parameters kept constant. Table S2 presents an overview of the dataset used for this case, displaying sample rows of doses of the catalyst, associated fixed conditions, and experimental degradation results. The comparison of the models' performance is

Table 2 Performance comparison of multiple ML models in predicting degradation efficiency across different pH levels

	Training set			Testing set		
Model	*R*2	RMSE	MAE	*R*2	RMSE	MAE
Decision Tree	0.981	2.162	1.427	0.917	4.588	4.222
Random Forest	0.958	3.243	2.729	0.793	7.180	5.637
ANN	0.983	2.033	1.458	0.904	4.898	4.178

Table 3 Actual *versus* predicted degradation efficiency under optimized conditions of pH by the decision tree model

Dye	Predicted value (%)	Actual value (%)	Difference (%)
CV	93.50	95.00	1.50
CR	93.50	92.00	1.50

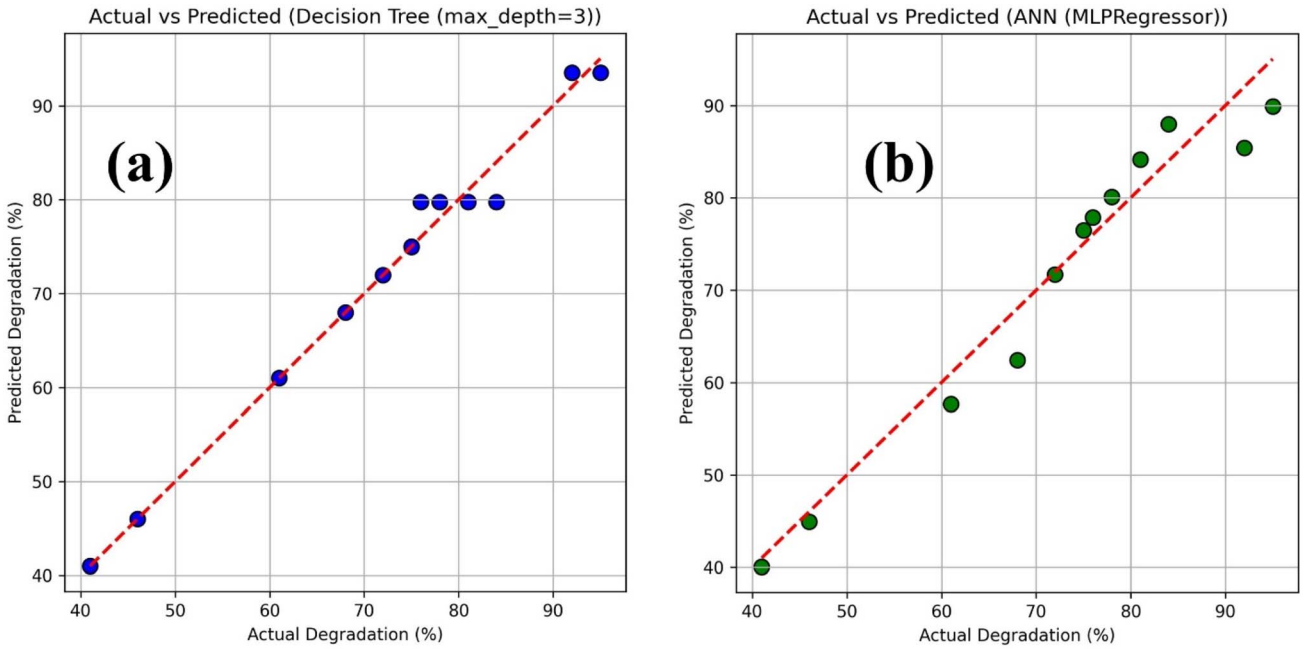

Fig. 11 Actual *vs.* predicted degradation efficiency (%) plots of the best-performing models for the pH optimization: (a) Decision Tree model, (b) ANN model.

illustrated in Table S3 and Fig. S2, which shows the best fitting of the decision tree model. Table 4 showed the comparison of predicted and observed degradation efficiencies of CV and CR dyes under optimized catalyst dose settings, as ascertained by the decision tree model. The findings indicated that the model closely aligns with experimental results, exhibiting slight deviations of 4.25% for CV and 1.25% for CR. This minor variation signifies that the model accurately reflects the impact of catalyst dosage on dye degradation performance, exhibiting commendable prediction accuracy and reliability.

To better demonstrate the predictability of the highest-performing (decision tree) as well as second-best models (random forest) for catalyst optimization, an Actual *vs.* Predicted graph were also plotted for each value, as shown in Fig. 12a (Decision Tree model) and Fig. 12b (Random Forest model).

Similarly, for the machine learning modelling of the initial dye concentration (ppm), the parameters, *i.e.*, pH and catalyst dosage, were kept constant. The data set comprises 10 rows with 6 columns, out of which the initial dye concentration was changed while the rest of the parameters were kept constant. Table S4 shows the preview of the data set utilized for this case, depicting sample rows of the initial dye concentration, corresponding conditions, and experimental degradation outcomes.

Table 4 Actual *versus* predicted degradation efficiency under optimized conditions of catalyst dosage by the decision tree model

Dye	Predicted value (%)	Actual value (%)	Difference (%)
CV	90.75	95.00	4.25
CR	90.75	92.00	1.25

The performance of the models is shown in Table S5 and Fig. S3, which shows the best fitting of the ANN (MLP) model. At optimized dye concentration, the degree of agreement between predicted and actual values is depicted in Table 5. The ANN model demonstrated excellent predictive performance, with minimal differences of 1.16% for CV and 0.10% for CR, indicating a high level of accuracy and strong correlation between predicted and experimental degradation efficiencies.

To better demonstrate the predictability of the highest-performing (ANN) as well as second-best (decision tree) models for the initial dye concentration optimization, an actual *vs.* predicted graph were also plotted for each value, as shown in Fig. 13a (ANN model) and Fig. 13b (Decision Tree model).

3.8. Total organic carbon content and reusability analyses

The extent of mineralization of CV and CR dyes by g-ZnO-NiO NCs was evaluated through TOC measurements (Fig. 14a). The TOC removal increased steadily with irradiation time, indicating progressive breakdown of dye molecules into smaller, less complex organic intermediates, followed by mineralization into CO_2, H_2O, and inorganic ions. After 5 hours of solar irradiation, the TOC removal efficiencies reached 84% for CV and 80% for CR, indicating that the photocatalyst achieved both effective decolorization and significant mineralization of the dyes. The marginally higher mineralization efficiency observed for CV can be attributed to its simpler aromatic structure, whereas the more complex diazo configuration of CR tends to generate more stable intermediate compounds during degradation. These findings demonstrate the strong performance of the Z-scheme heterojunction in maintaining active oxidative and reductive species over extended irradiation, thereby facilitating thorough pollutant mineralization.

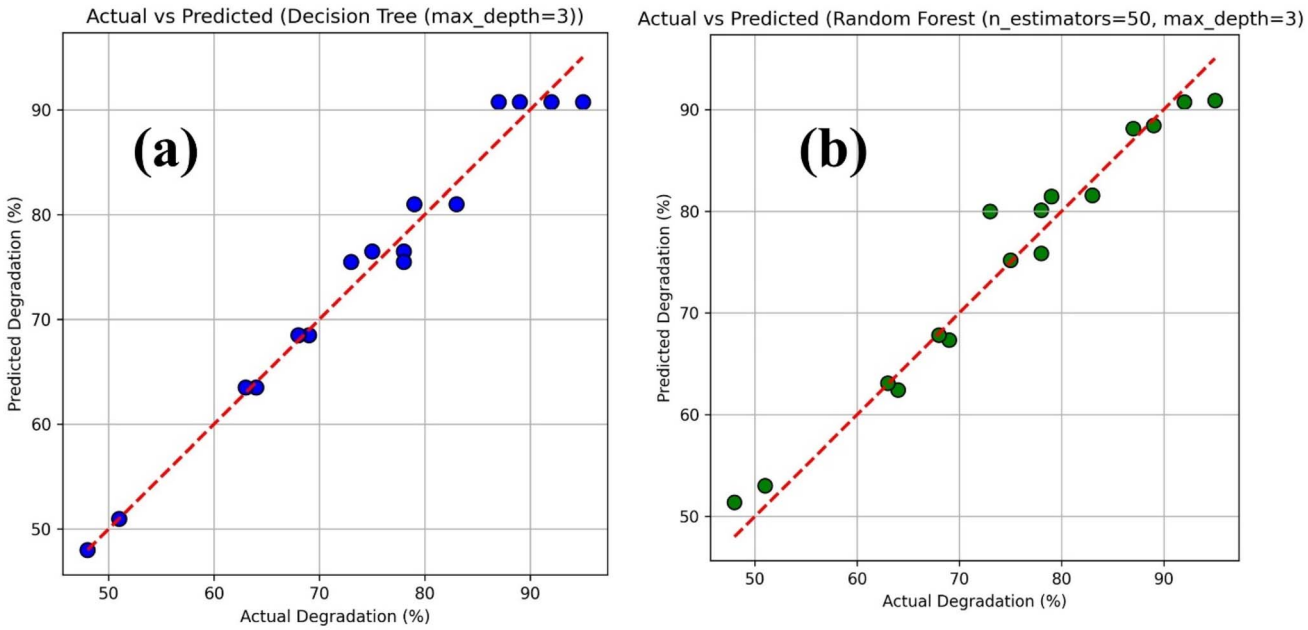

Fig. 12 Actual *vs.* predicted degradation efficiency (%) plots of the best-performing models for the catalyst optimization: (a) Decision Tree model, (b) Random Forest model.

Table 5 Actual *versus* predicted degradation efficiency under optimized conditions of dye concentration by the ANN (MLP) model

Dye	Predicted value (%)	Actual value (%)	Difference (%)
CV	93.84%	95.00%	1.16%
CR	91.90%	92.00%	0.10%

The reusability of g-ZnO-NiO NCs was evaluated through five successive photocatalytic cycles for the degradation of CV and CR (Fig. 14b). Only a slight reduction in efficiency was noted, with CV removal decreasing from 95% to 89% and CR removal from 92% to 86% after the 5th run. This minor decline in activity is likely due to partial catalyst loss during recovery, surface contamination from adsorbed intermediates, or slight

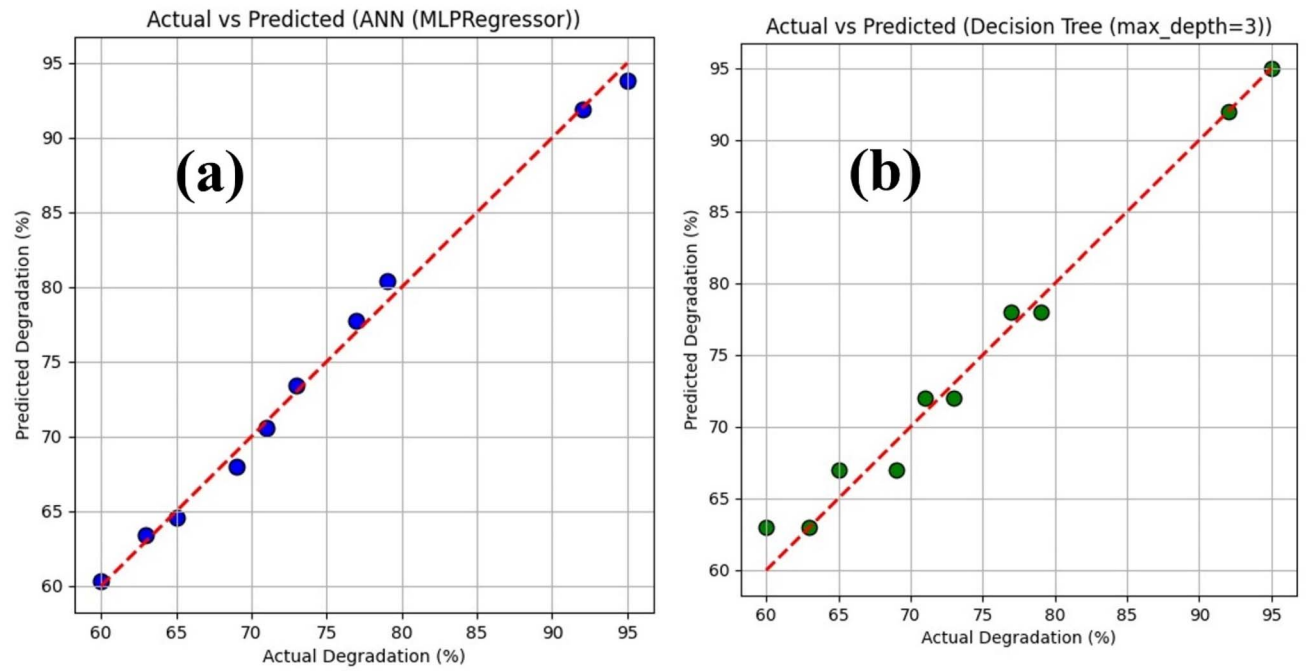

Fig. 13 Actual *vs.* predicted degradation efficiency (%) plots of the best-performing models for the initial dye concentration: (a) ANN model, (b) Decision Tree model.

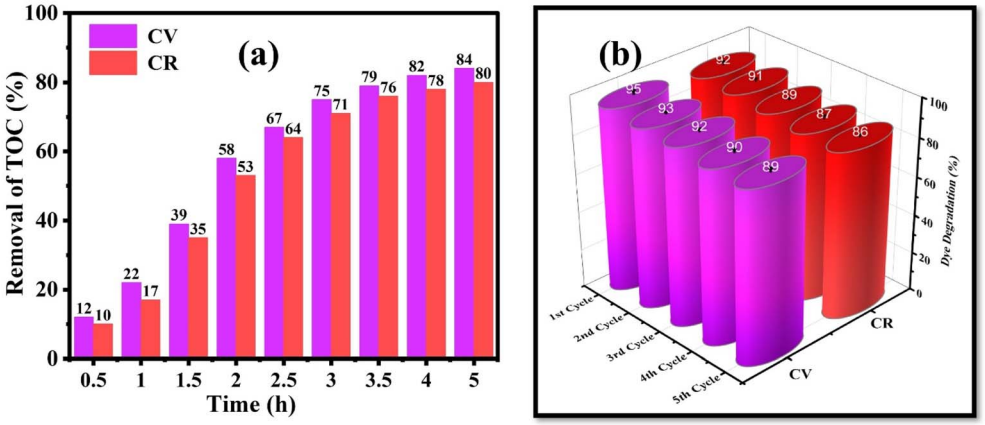

Fig. 14 (a) Extent of mineralization of dye molecules by TOC analysis and (b) reusability studies of g-ZnO-NiO NCs.

alterations in surface active sites. Despite this, the strong retention of photocatalytic performance across multiple cycles underscores the excellent stability and durability of the GA-capped Z-scheme NCs, affirming their potential for real-world wastewater treatment applications.

3.9. Antioxidant potential of g-ZnO NPs, g-NiO NPs, and g-ZnO-NiO NCs

GA is well known to possess antioxidant power of the neutralization of ROS and free radicals by the donation of hydrogen atoms or electrons through the aid of several hydroxyl groups. This property is important in decreasing the oxidative stress, which plays a major role in the prevention of inflammation, cell damage, and other chronic diseases, including cancer, heart disease, and neurodegenerative disorders. In the case of its application as a capping agent, GA has the capacity to alter the antioxidant characteristics of NPs and NCs as demonstrated by the outcomes of the TPC, FRAP, and DPPH assays (Fig. 15). The testing of GA-capped NPs by the use of these assays showed that there was a concentration dependent rise in antioxidant activity

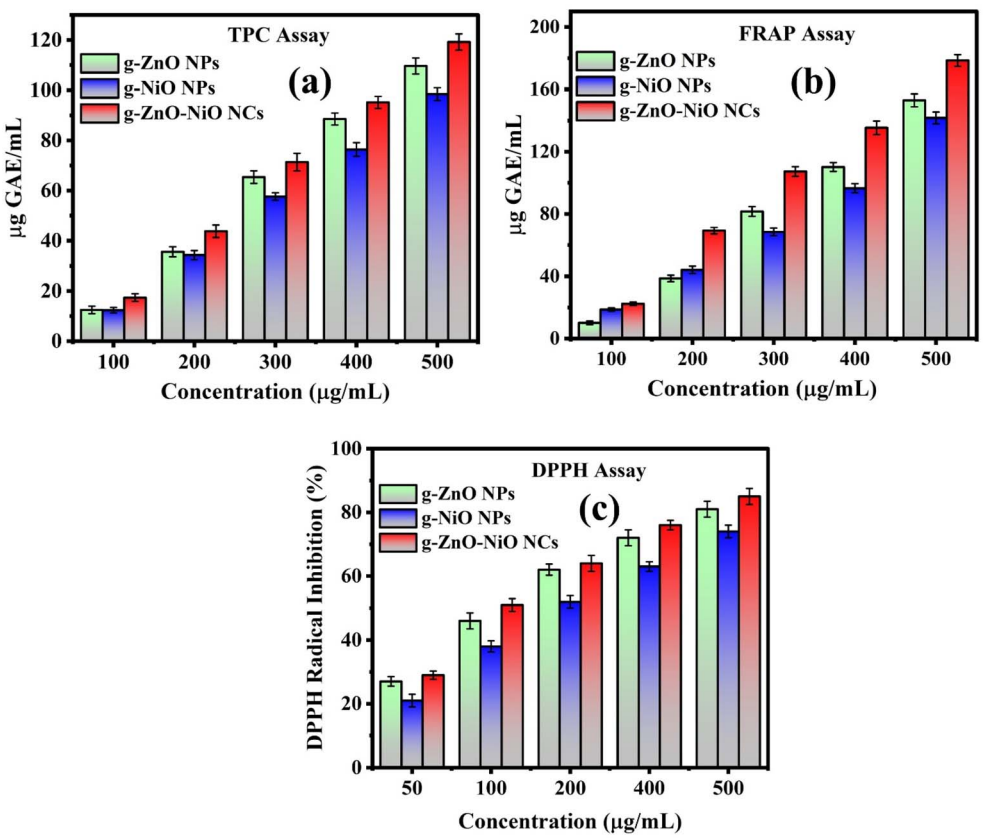

Fig. 15 Antioxidant activity results of g-ZnO NPs, g-NiO NPs, and g-ZnO-NiO NCs by: (a) TPC assay, (b) FRAP assay, and (c) DPPH assay.

in all the samples analyzed. g-ZnO NPs and g-NiO NPs demonstrated a high level of phenolic content, equal to 109.6 ± 3.2 and 98.5 ± 2.5 μg_{GAE} mL^{-1} at a concentration of 500 μg mL^{-1}, respectively, as illustrated in Fig. 15a. Meanwhile the g-ZnO-NiO NCs showed the highest phenolic content of almost 119.2 ± 3.5 μg_{GAE} mL^{-1}. Similarly, in the FRAP assay, the g-ZnO NPs have shown higher reducing power than the g-NiO NPs. The reducing strengths shown by g-ZnO NPs and g-NiO NPs were 153 ± 4.2 and 141.7 ± 3.8 μg_{GAE} mL^{-1}, respectively. The highest reducing power of 178.5 ± 2.5 μg_{GAE} mL^{-1} was shown by the g-ZnO-NiO NCs, as depicted in Fig. 15b. In addition, the DPPH radical scavenging activity supported the high level of antioxidant activity exhibited by the g-ZnO-NiO NCs, with 85 ± 2.5% inhibition of DPPH radical as compared to the g-ZnO NPs (81 ± 2.0%) and g-NiO NPs (74 ± 1.5%) at the same concentration, as shown in Fig. 15c. The high antioxidant activity of the g-ZnO-NiO NCs in all the assays was attributed to the synergies between g-ZnO and g-NiO that enhance the reactive surface area and charge transfer dynamics between the two in NCs. Further, the capping and stabilizing effect of GA is also vital, since it adds a vast amount of hydroxyl groups, which not only increase the phenolic content and radical-scavenging effect but also avoid the agglomeration of NPs. The results described here demonstrated that GA functionalization has a great contribution in improving the natural antioxidant properties of the metal oxide nanoparticles and enabling the nanocomposites to perform better as compared to the individual component nanoparticles. In conclusion, the g-ZnO-NiO NCs are the most efficient antioxidant material and may be considered for treating oxidative stress.

4. Conclusion

Gallic acid-capped ZnO nanoparticles, NiO nanoparticles, and their Z-scheme g-ZnO-NiO nanocomposites were successfully synthesized through a green synthesis route and exhibited remarkable photocatalytic performance for degrading CV and CR dyes under solar illumination. The g-ZnO-NiO nanocomposites outperformed the individual oxides, achieving up to 95% and 92% degradation of CV and CR, respectively, with corresponding rate constants of 2.84×10^{-2} min^{-1} and 2.56×10^{-2} min^{-1}, along with high mineralization efficiencies of 84% and 80%. The enhanced photocatalytic activity was ascribed to efficient charge separation and strong redox potential enabled by the Z-scheme heterojunction, which promoted the formation of highly reactive $^{\bullet}O_2^-$ and $^{\bullet}OH$ radicals. The catalyst maintained excellent stability and reusability over repeated cycles, underscoring its suitability as a sustainable and durable photocatalyst for wastewater treatment. Furthermore, machine learning models effectively simulated the photocatalytic degradation behavior of CV and CR under various experimental parameters. Among the models tested, Decision Tree, ANN, and Random Forest demonstrated the highest predictive accuracy, confirming the potential of ML-based approaches to optimize reaction conditions and support experimental design in photocatalysis. The antioxidant studies revealed the higher antioxidant potential of g-ZnO-NiO NCs, as evidenced by their high TPC (119.2 ± 3.5 μg_{GAE} mL^{-1}), FRAP (178.5 ± 2.5 μg_{GAE} mL^{-1}), and DPPH radical scavenging power (85 ± 2.5%), as compared to g-ZnO NPs and g-NiO NPs.

Author contributions

Aqeela Sikandar and Abu Bakar Siddique: methodology, investigation, writing – original draft, and writing – review & editing. Azhar Abbas and Abdul Majid: conceptualization, investigation, and writing – review & editing. Bilal Sikandar and Muhammad Asharf Shaheen: methodology and writing – review & editing. Umar Nishan and Khaled Fahmi Fawy: investigation, resources, and writing – review & editing.

Conflicts of interest

The authors have no known financial or non-financial interests to disclose.

Data availability

All evaluated data are available in the manuscript. Additional information/data can be provided upon reasonable request.

Supplementary information is available. See DOI: https://doi.org/10.1039/d5na00827a.

Acknowledgements

The authors extend their appreciation to the Deanship of Research and Graduate Studies at King Khalid University, Saudi Arabia, through the Large Research Project under grant number RGP-2/685/46.

References

1 S. A. Bahadi, Q. Drmosh and S. A. Onaizi, *Sep. Purif. Technol.*, 2024, **337**, 126402.
2 H. R. Dihom, M. M. Al-Shaibani, R. M. S. R. Mohamed, A. A. Al-Gheethi, A. Sharma and M. H. B. Khamidun, *J. Water Process Eng.*, 2022, **47**, 102705.
3 F. S. Mustafa and A. A. Oladipo, *J. Water Process Eng.*, 2024, **64**, 105686.
4 A. Nezamzadeh-Ejhieh and Z. Banan, *Desalination*, 2011, **279**, 146–151.
5 A. Nezamzadeh-Ejhieh and Z. Banan, *Desalination*, 2012, **284**, 157–166.
6 A. Nezamzadeh-Ejhieh and M. Karimi-Shamsabadi, *Chem. Eng. J.*, 2013, **228**, 631–641.
7 A. Nezamzadeh-Ejhieh and H. Zabihi-Mobarakeh, *J. Ind. Eng. Chem.*, 2014, **20**, 1421–1431.
8 M. Sagir, M. B. Tahir, J. Akram, M. S. Tahir and U. Waheed, *Curr. Anal. Chem.*, 2021, **17**, 38–48.
9 H. Ahmad, A. B. Siddique, S. Zaheer, R. Sattar, A. Abbas, M. Amin, R. Al-Salahi, H. A. Abuelizz and M. Z. Saleem, *J. Water Process Eng.*, 2025, **74**, 107855.
10 A. B. Siddique, M. A. Shaheen, S. Shafeeq, A. Abbas, Y. Zaman, Z. Ishaque and M. Aslam, *Mater. Adv.*, 2025, **6**, 1330–1344.

11 A. Nezamzadeh-Ejhieh and S. J. Khorsandi, *J. Ind. Eng. Chem.*, 2014, **20**, 937–946.
12 A. Yousefi and A. Nezamzadeh-Ejhieh, *Iran. J. Catal.*, 2021, **11**, 247–259.
13 M. Rezaei, A. Nezamzadeh-Ejhieh and A. R. Massah, *Energy Fuels*, 2024, **38**, 8406–8436.
14 M. Rezaei, A. Nezamzadeh-Ejhieh and A. R. Massah, *ACS Omega*, 2024, **9**, 6093–6127.
15 R. R. Chandrapal and G. Bakiyaraj, *Water, Air, Soil Pollut.*, 2024, **235**, 376.
16 N. Omrani and A. Nezamzadeh-Ejhieh, *J. Photochem. Photobiol., A*, 2020, **389**, 112223.
17 R. Fazaeli, H. Aliyan, A. Nezamzadeh-Ejhieh and D. J. S. Richeson, *Surf. Interfaces*, 2024, **52**, 104877.
18 S. Salesi and A. Nezamzadeh-Ejhieh, *Environ. Sci. Pollut. Res.*, 2023, **30**, 105440–105456.
19 P. Abisha, C. Jinitha and S. Sonia, *Physica E*, 2025, **165**, 116076.
20 N. R. Reddy, P. M. Reddy, J. H. Jung and S. W. Joo, *Inorg. Chem. Commun.*, 2022, **146**, 110107.
21 J. Wu, X. Yue, T. Wang, Y. Zhang, Y. Jin and G. Li, *Colloids Surf., A*, 2025, **717**, 136850.
22 L. Dong, J. Ding, L. Zhu, Y. Liu, X. Gao and W. Zhou, *Chin. Chem. Lett.*, 2023, **34**, 108192.
23 M. Yi, Y. Ren, X. Zhang, Z. Zhu and J. Zhang, *J. Colloid Interface Sci.*, 2024, **658**, 334–342.
24 P. Guo, Y. Wu, X. Ma, R. Chen, Z. Zeng, L. Li, C. Su and S. Wang, *Appl. Surf. Sci.*, 2025, 163754.
25 A. B. Siddique, M. A. Shaheen, A. Abbas, Y. Zaman, M. U. Rasheed, A. Karim, M. Mustaqeem, M. M. Alam and A. S. Alahmari, *Water, Air, Soil Pollut.*, 2025, **236**, 1–22.
26 M. Ahani and M. Khatibzadeh, *Inorg. Nano-Met. Chem.*, 2022, **52**, 234–240.
27 L.-Y. Wang, M.-Y. Wu, Z.-Y. Wu and Y.-T. Li, *J. Mol. Struct.*, 2025, 143355.
28 M. Khan, F. Ahmad, J. T. Koivisto and M. Kellomäki, *Colloid Interface Sci. Commun.*, 2020, **39**, 100322.
29 J. M. Lee, K.-H. Choi, J. Min, H.-J. Kim, J.-P. Jee and B. J. Park, *Nanomaterials*, 2017, **7**, 365.
30 Y. Deligiannakis, G. A. Sotiriou and S. E. Pratsinis, *ACS Appl. Mater. Interfaces*, 2012, **4**, 6609–6617.
31 J. Xing, H. Wang, K. Luo, S. Wang, Y. Bai and J. Fan, *Renewable Energy*, 2019, **136**, 104–114.
32 D. M. Basavarajaiah and B. N. Murthy, in *Design of Experiments and Advanced Statistical Techniques in Clinical Research*, Springer, 2020, pp. 133–156.
33 Y. Ahmed, K. R. Dutta, S. N. C. Nepu, M. Prima, H. AlMohamadi and P. Akhtar, *Results Eng.*, 2025, **25**, 103538.
34 A. B. Siddique, M. A. Shaheen, A. Abbas, Y. Zaman, H. M. Amin, M. M. Alam, N. K. Alharbi, F. Alshehri, A. Shami and F. A. Al-Joufi, *Int. J. Environ. Anal. Chem.*, 2025, **1**, 1–23.
35 S. Ghattavi and A. Nezamzadeh-Ejhieh, *Int. J. Hydrogen Energy*, 2020, **45**, 24636–24656.
36 J. Vera, W. Herrera, E. Hermosilla, M. Díaz, J. Parada, A. B. Seabra, G. Tortella, H. Pesenti, G. Ciudad and O. Rubilar, *Antioxidants*, 2023, **12**, 784.
37 Z. Bedlovičová, I. Strapáč, M. Baláž and A. Salayová, *Molecules*, 2020, **25**, 3191.
38 A. B. Siddique, M. A. Shaheen, A. Abbas, Y. Zaman, M. A. Bratty, A. Najmi, A. Hanbashi, M. Mustaqeem, H. A. Alhazmi and Z. ur Rehman, *Heliyon*, 2024, **10**, e40679.
39 M. Tariq, Y. Zaman, M. Shahzad, K. Ahmad, A. B. Siddique and H. Zaman, *Mater. Sci. Eng., B*, 2023, **294**, 116549.
40 A. H. Aseen, V. Gowthami, P. Jyolsna and J. Integr, *Sci. Technol.*, 2025, **13**, 1056.
41 A. B. Siddique, M. A. Shaheen, A. Abbas, Y. Zaman, M. Z. Ishaque, A. Shami, M. Aslam, K. M. Alsyaad and A. Ali, *J. Mol. Struct.*, 2025, **1331**, 141566.
42 A. B. Siddique, M. A. Shaheen, A. Abbas, Y. Zaman, A. Ali, M. Naeem-ul-Hassan and J. Iqbal, *J. Environ. Chem. Eng.*, 2024, **12**, 112725.
43 N. Arabpour and A. Nezamzadeh-Ejhieh, *Process Saf. Environ. Prot.*, 2016, **102**, 431–440.
44 T. Tamiji and A. Nezamzadeh-Ejhieh, *Mater. Chem. Phys.*, 2019, **237**, 121813.
45 H. K. Abid, A. B. Siddique, A. Abbas, M. A. Shaheen, A. Ali, M. Fatima, A. Shami, M. A. Alrayyani, F. A. Al-Joufi and M. A. Assiri, *Nanoscale Adv.*, 2025, **7**, 6145–6157.
46 A. Noruozi and A. Nezamzadeh-Ejhieh, *Chem. Phys. Lett.*, 2020, **752**, 137587.
47 S. Senobari and A. Nezamzadeh-Ejhieh, *J. Mol. Liq.*, 2018, **261**, 208–217.
48 N. Omrani and A. Nezamzadeh-Ejhieh, *J. Mol. Liq.*, 2020, **315**, 113701.
49 Z. Khalid, A. Ali, A. B. Siddique, Y. Zaman, M. F. Sibtain, A. Abbas, M. M. Alam and M. S. Alwethaynani, *RSC Adv.*, 2025, **15**, 16879–16893.
50 A. B. Siddique, M. A. Shaheen, A. Abbas, S. Akhtar, M. Shahzad, A. Ali, N. Ahmad, H. A. Abuelizz and R. Al-Salahi, *Fuel*, 2026, **406**, 137178.
51 S. Sharafzadeh, J. Zolgharnein, A. Nezamzadeh-Ejhieh and S. D. Farahani, *Int. J. Hydrogen Energy*, 2025, **106**, 1429–1442.
52 A. N. Ejhieh and M. Khorsandi, *J. Hazard. Mater.*, 2010, **176**, 629–637.
53 A. Sobhani-Nasab, M. Eghbali-Arani, S. M. Hosseinpour-Mashkani, F. Ahmadi and M. Rahimi-Nasrabadi, *Iran. J. Catal.*, 2020, **10**, 91–99.
54 A. Pourtaheri and A. Nezamzadeh-Ejhieh, *Chem. Eng. Res. Des.*, 2015, **104**, 835–843.
55 F. S. Mustafa, A. A. Oladipo and M. Gazi, *ChemistrySelect*, 2022, **7**, e202200727.
56 A. Nezamzadeh-Ejhieh and S. Hushmandrad, *Appl. Catal., A*, 2010, **388**, 149–159.
57 A. Nezamzadeh-Ejhieh and Z. Shams-Ghahfarokhi, *J. Chem.*, 2013, **2013**, 104093.
58 S. A. Mirsalari and A. Nezamzadeh-Ejhieh, *Sep. Purif. Technol.*, 2020, **250**, 117235.
59 P. Hemmatpour and A. Nezamzadeh-Ejhieh, *Chemosphere*, 2022, **307**, 135925.
60 S. A. Mirsalari, A. Nezamzadeh-Ejhieh and A. R. Massah, *Spectrochim. Acta, Part A*, 2023, **288**, 122139.